Graphical Abstract

Quasi-brittle porous material: simulated effect of stochastic air void structure on compressive strength

Anna-Leena Erkkilä, Teemu Leppänen, Jussi Virkajärvi, Joni Parkkonen, Leena Turunen, Tero Tuovinen

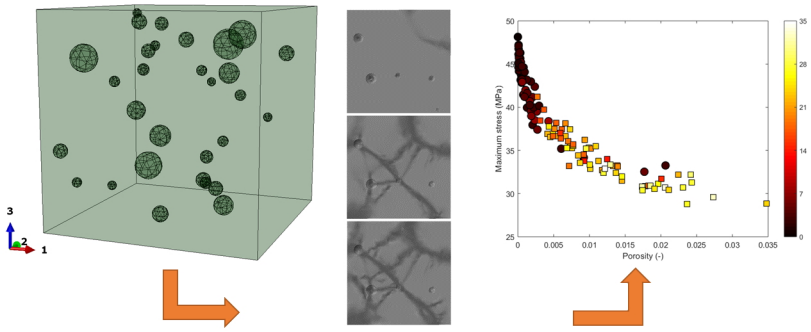

Highlights

Quasi-brittle porous material: simulated effect of stochastic air void structure on compressive strength

Anna-Leena Erkkilä, Teemu Leppänen, Jussi Virkajärvi, Joni Parkkonen, Leena Turunen, Tero Tuovinen

- A simulation procedure to investigate the effect of porosity comprised of spherical air voids on the compressive strength of a quasi-brittle material is introduced.
- Based on the simulated results, the relationship between compressive strength and air void fraction (porosity) is presented.
- A linear relationship was achieved between the cubic root of porosity and the simulated compressive strength.

Quasi-brittle porous material: simulated effect of stochastic air void structure on compressive strength

Anna-Leena Erkkilä[a], Teemu Leppänen[a], Jussi Virkajärvi[b], Joni Parkkonen[b], Leena Turunen[c], Tero Tuovinen[c,*]

[a] *Faculty of Information Technology, University of Jyväskylä, Finland*
[b] *Department of Physics, University of Jyväskylä, Finland*
[c] *School of Technology, Jyväskylä University of Applied Sciences, Finland*

Abstract

The effect of porosity comprised of spherical air voids on the compressive strength of quasi-brittle material was studied via simulations. The simulated porous structures were based on pore size distributions of two mortar samples measured by X-ray microtomography. While the simulation method set practical limits on the size of sample, the base of the statistics was established by simulating 128 small structures generated by sampling from pore structures of two mortars. By studying the application of the classical strength-porosity formulas to the simulated data, a new simple model was formed. A linear relationship was achieved between the cubic root of air void fraction (porosity) and the simulated compressive strength. The reasons for scattering of simulated strength around fitted trend remained unresolved in this study; no clear dependence on pore number or other distribution properties was observed. With the presented simulation approach, the dependence of compressive strength on porosity is achieved independently of disturbances

*Corresponding author.
Email address: tero.tuovinen@jamk.fi (Tero Tuovinen)

that occur in experimental studies creating understanding of compressional behavior of low porosity materials.

Keywords: Porosity, Mortar, Compressive strength, Finite element method, Simulation, Model

---

1. Introduction

The strength and behavior of a material depends on its internal structure. In particular, in the case of a porous material, it is known that porosity affects strongly e.g. elastic modulus, yield behavior and tensile and compressive strength. Concrete and other cement-based materials are widely used porous materials where porosity has a crucial role in the suitability of the materials for their numerous uses. For this reason, and in addition to the need to make these materials more environmentally friendly by utilizing additives, the effect of the porosity on the behavior of the material has been extensively studied for several decades. The importance of porosity, pore distribution and potential additives for the compressive strength of cement-based materials has been clarified in several studies, see for example, [1–10]. These studies have shown that porosity has a strong effect on compressive strength and, in addition, in the case of additives, changes in compressive strength come at least in part due to a change in porosity. The phenomenological, experiment based, equations introduced by Balshin [11], Ryshkewitch [12], Schiller [13] and Hasselman [14] have been utilized to describe the dependence of the compressive strength of cement-based materials on porosity for decades. Analytical approaches have also been developed to describe this dependence [15, 16].

The pores of cement-based materials are often classified into different categories based on their size and type: e.g. gel ($<$ 10 nm), capillary (0.005 - 10 μm), and air (macropores 0.005 - 5 mm) pores. Also, the cracks due to shrinkage at aggregate-cement interface are common. The ranges of pore categories are not strictly defined and different sources cite slightly different ranges, see, e.g., [17–23]. Capillary pores and other larger pores are found to be responsible for reduction in strength of cement paste, while the effect of gel pores are noticed to be negligible [1, 4]. Several measurement methods have been applied to the porous structure characterization of cement-based materials, such as mercury intrusion porosimetry (MIP), vapor sorption, scanning electron microscopy, and X-ray tomography. Frequently used mercury intrusion as well as vapor sorption techniques are indirect methods, which means that the interpretation of the results usually requires some assumptions and theoretical simplifications [24–27]. Mercury intrusion technique allows pore sizes over a broad range to be measured, whereas the vapor sorption techniques are more sensitive to gel scale pores. In MIP, the closed pores remain nonintruded, while for those large pores, which are only accessible by very narrow throats, the size is misinterpreted; this mechanism is commonly referred to as the "ink bottle" effect [22]. To observe a direct physical structure of the microstructure different imaging techniques have been utilized. Scanning electron microscopy produce images of microstructure features from 2D cross sections with resolution of submicron ranging from capillar porosity scale [23, 28, 29]. For the acquisition of 3D information of the pores, some studies using X-ray computed tomography have been presented [30–32]. Micro-tomography provides resolution in the order of few microns.

In recent decades, the finite element method has been extensively utilized in the study of the behavior of cement-based heterogeneous materials. These studies are focused on, e.g., the dependence of the elastic properties on the aggregate content and on the shape and distribution of the aggregate, see for example, [33, 34]. In addition to the elastic properties, the strength and fracture behavior of the material and its dependence on aggregate properties have been considered, e.g., in references [35–39]. The most common approach in these studies is to divide the cement-based material into the cement matrix, the aggregate, and the interfacial transaction zone, each of which has its own material properties. In addition to the effect of aggregate, the effect of porosity on the mechanical behavior of cement-based material has also been studied by the finite element method [40, 41] and by the discrete element method [42].

This paper aims to investigate the effect of variations in porous structure on the compressive strength of quasi-brittle material through a numerical approach. X-ray microtomography was used to determine 3D pore structure of two mortar samples, without and with 10 % green liquor dregs (GLD). GLDs, which are a side streams of pulping mills containing environmentally hazardous metals, are a recycling challenge. Its treatment and recycling are under investigation by several parties. However, in this study, the role of GLD as an additive of mortar is limited to the generation of different structures for porosity studies. To simulate the compressive strength, 128 cubes with the sides of 0.5 mm and different pore volume ratios, distributions and positionings were constituted based on the measured pore size distributions. Due to the cube size of the simulations and the measurement resolution the

pore sizes were limited to between 20 μm and 500 μm. The statistically relevant number of pore structures was used in the simulations to reveal the dependence of compressive strength solely on porosity, without interference with other factors due to composition and manufacturing process.

2. Pore structures

2.1. Preparation of mortar samples

Mortar samples with dimensions 40 mm x 40 mm x 160 mm were prepared according to the standard EN 196-1. Two different mortars were produced: Sample 1 consisted of CEN standard sand, water and cement and in Sample 2 10 % of cement weight was replaced by dried and milled green liquor dregs. The six parallel samples with size approximately 5 mm $\times$ 5 mm $\times$ 5 mm were cut from the produced samples.

2.2. X-ray tomography imaging and image analysis

Internal 3D-structure of mortar samples was measured using SkyScan 1172 X-ray microtomographic scanner; examples about measured cross-sections are shown in Fig. 1. X-ray source parameters of 85 kV and 82 μA were used and Al+Cu plate was placed in front of the detector to filter out low X-ray energies. Camera pixel binning 2 $\times$ 2 was applied resulting in image pixel size of 5.0 μm. Exposure time for a single frame was 3540 ms and average over 4 frames was taken for each projection. Full rotation of 360° was made with 0.3° rotation step resulting in 1200 projection images. The scan duration was 6 hours. Tomographic reconstructions were made using NRecon software, which applies Feldkamp algorithm [43].

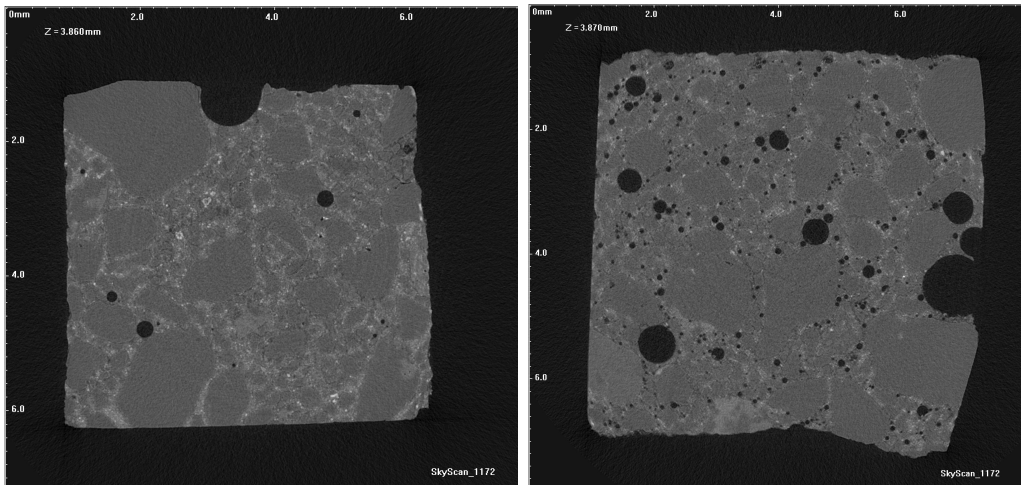

Figure 1: X-ray microtomography cross-sections from Sample 1 (left) and Sample 2 (right). The size of the measured samples was approximately 5 mm $\times$ 5 mm $\times$ 5 mm.

Pore volumes where determined from the tomography images using Fiji [44] and Matlab softwares. Two different croppings were performed for the original sample image. One of the cropped images included the whole sample and the other a smaller box-shaped volume from inside the sample. Fiji build-in 3D Gaussian filter with standard deviation $\sigma_i^G = 1$ for all $i \in \{x, y, z\}$ was applied for both cropped images. The pore space was segmented using Fiji build-in Otsu auto thresholding. The segmented pores, in the larger cropped images, which were not completely inside the sample but touched the exterior background, were read as background and thus were not included in the pore analysis.

From all the images a relative porosity was calculated. The porosity results from the smaller cropped images were used for consistency checks. Matlab DIPimage [45] watershed was used for the pore structural segmen-

tation. Inverted distance transform images, produced from the pore binary images, provided base geometry for watershed. Sizes of individual pores were measured after pore labeling for the larger cropped images. As 18-connected neighborhood was used in watershed analysis, moderate under-segmentation of pore structures was observed. For example, not all larger connected pores were segmented properly, on the other hand some smaller "non-spherical" voids, like cracks, were not over-segmented either. These cause moderate distortion in the pore distributions mainly by reducing the total number of pores and increasing the number of larger pores while decreasing the number of smaller ones. Results determined for pore-like objects smaller than 50 voxels can be considered unreliable due to mixing with noise. This also means that capillary pores are not taken into account in the present study, and thus the porosity refers to air voids here only.

2.3. Structures for simulation

For each sample, the X-ray tomography results of six parallel samples were merged. The porosity distributions obtained for Sample 1 and Sample 2 are shown in Fig. 2 and the statistical properties of distributions are given in Table 1. Due to the measurement noise, pores with a radius of less than 10 μm (pore-like objects less than 34 voxels) are excluded from consideration. Cubes of equivalent volume to the total volumes of parallel samples were formed having side length of 9.6 mm for Sample 1 and 10.0 mm for Sample 2. Since the pores studied consisted mainly of air-voids, the shape of the sphere is a suitable approximation for simulations. The measured individual pores were randomly placed inside the volume-equivalent cubes as volume-equivalent spheres. For the simulations, subcubes with a side length of 0.5

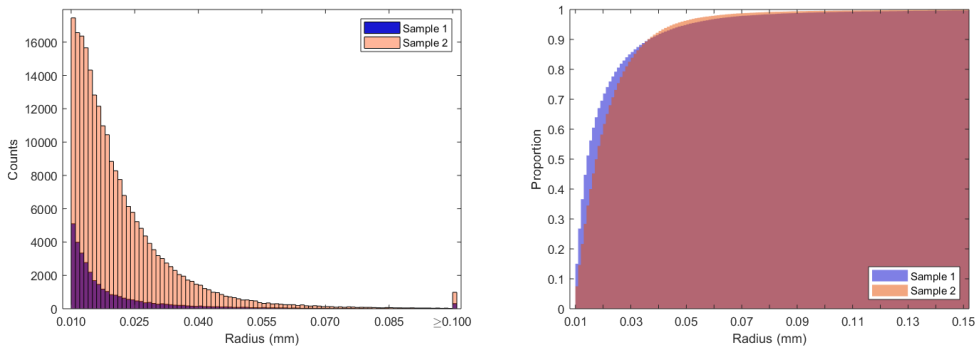

Figure 2: Pore radius distributions related to Sample 1 and Sample 2. The overlap of the distributions is shown in a mixed color.

mm were picked from porous volume-equivalent cubes at the points of a regular 8×8 grid. Thus, for both samples, 64 subcubes were produced for simulations. Details of subcubes are given in Tables A.5 and A.6 (Appendix). A single subcube based on Sample 1 is referred to as $\mathrm{S1}_\gamma \in \mathrm{S1}$ and the subcube of Sample 2 is referred to as $\mathrm{S2}_\gamma \in \mathrm{S2}$ ($\gamma = 1, 2, \ldots, 64$), respectively. Only pores that remained completely inside the subcube were accepted. This means that pores with a radius greater than 0.25 mm are not included in the study. Because the largest pores are excluded from the study, the mean values of pore volume of the subcubes remains, on average, clearly lower than the mean values of measured porosity presented in Table 1. Sampling also resulted in four subcubes of data set S1 with no pores. An example of subcube is illustrated in Fig. 4.

Table 1: Data of Sample 1 and Sample 2; pores with $r < 10$ μm are excluded. Symbols V, r and N stands for volume, pore radius and number of pores, respectively.

Sample	1	2
Cube side dimension (mm)	9.60	10.00
Mean r (mm)	0.0211	0.0221
Median r (mm)	0.0148	0.0180
Mean pore V (mm^3)	6.0471e-04	1.8482e-04
Median pore V (mm^3)	1.3627e-05	2.4430e-05
N	33943	232939
Mean N in $V = 0.5^3$ mm^3	4.7956	29.1174
Porosity (%)	2.32	4.30
N ($r \geq 250$ μm)	34	54
Mean N ($r \geq 250$ μm) in $V = 0.5^3$ mm^3	0.0048	0.0068
Porosity ($r \geq 250$ μm) (%)	1.53	0.94

3. Constitutive model

The constitutive model used is the damaged plasticity model available in Abaqus [46]. The original model is presented in the reference [47] and its modifications in the reference [48]. The stress-strain relation is governed by

$$\sigma = (1 - d) D_0^{el} (\varepsilon - \varepsilon^{pl}) \tag{1}$$

where σ, d, D_0^{el}, ε and ε^{pl} are the Cauchy stress, scalar stiffness degradation variable, undamaged elastic stiffness of the material, total strain and plastic strain, respectively. The stress-strain behavior corresponding to the undamaged ($d = 0$) material used in the model is shown in Fig. 3 with respect to tension and compression. In the elastic region, the material is defined

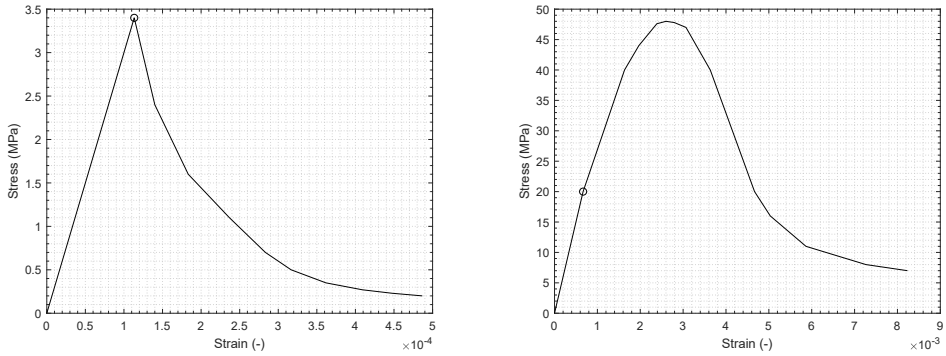

Figure 3: Stress-strain behavior of undamaged ($d = 0$) material for tension (left) compression (right). Stress and inelastic strain data is given in Table 2. The limiting point between elastic and inelastic regions is marked with 'o'.

by Young's modulus $E = 30$ GPa. Poisson ratio $\nu = 0.2$ does not depend on strain. Stress-strain behavior, Young's modulus and Poisson ratio are selected to represent typical behavior and values used for concrete [49, 50]. The total strain rate $\dot{\varepsilon}$ is assumed to be sum of the elastic part of the strain rate $\dot{\varepsilon}^{el}$ and the plastic part of the strain rate $\dot{\varepsilon}^{pl}$. The effective stress $\bar{\sigma}$ is defined as

$$\bar{\sigma} = D_0^{el}(\varepsilon - \varepsilon^{pl}) \tag{2}$$

and by Eq. (1) the Cauchy stress and the effective stress are related by

$$\sigma = (1 - d)\bar{\sigma}. \tag{3}$$

The scalar stiffness degradation variable $0 \leq d \leq 1$ is defined as

$$d = 1 - (1 - d_c)(1 - r(\hat{\bar{\sigma}})d_t) \tag{4}$$

where $0 \leq d_t \leq 1$ and $0 \leq d_c \leq 1$ are the uniaxial scalar stiffness degradation variables in tension and compression, respectively, and the stress weight factor $0 \leq r(\hat{\bar{\sigma}}) \leq 1$ is

$$r(\hat{\bar{\sigma}}) = \frac{\frac{1}{2}\sum_{i=1}^{3}(|\hat{\bar{\sigma}}_i| + \hat{\bar{\sigma}}_i)}{\sum_{i=1}^{3}|\hat{\bar{\sigma}}_i|} \tag{5}$$

where $\hat{\bar{\sigma}}_i$ are the eigenvalues of the effective stress.

Hardening variables, equivalent plastic strains in tension, $\tilde{\varepsilon}_t^{pl}$, and in compression, $\tilde{\varepsilon}_c^{pl}$, characterize the damaged states in tension and compression independently. The equivalent plastic strain rate $\dot{\tilde{\varepsilon}}^{pl}$ is defined as

$$\dot{\tilde{\varepsilon}}^{pl} = [\dot{\tilde{\varepsilon}}_t^{pl} \;\; \dot{\tilde{\varepsilon}}_c^{pl}]^T \tag{6}$$

where the plastic strain rates in tension $\dot{\tilde{\varepsilon}}_t^{pl}$ and compression $\dot{\tilde{\varepsilon}}_c^{pl}$ are

$$\dot{\tilde{\varepsilon}}_t^{pl} = r(\hat{\bar{\sigma}})\dot{\hat{\varepsilon}}_{\max}^{pl} \tag{7}$$

$$\dot{\tilde{\varepsilon}}_c^{pl} = -(1 - r(\hat{\bar{\sigma}}))\dot{\hat{\varepsilon}}_{\min}^{pl} \tag{8}$$

where $\hat{\varepsilon}_{\max}^{pl}$ and $\hat{\varepsilon}_{\min}^{pl}$ are the maximum and minimum eigenvalues of the plastic strain rate $\dot{\varepsilon}^{pl}$, respectively. The stiffness degradation variables d_t and d_c in Eq. (4) are selected so that

$$\tilde{\varepsilon}_t^{pl} = \tilde{\varepsilon}_t^{in}/2 \tag{9}$$

$$\tilde{\varepsilon}_c^{pl} = \begin{cases} \tilde{\varepsilon}_c^{in} & \text{when} \quad d_c = 0 \\ \tilde{\varepsilon}_c^{in}/2 & \text{when} \quad d_c > 0 \end{cases} \tag{10}$$

Table 2: Stresses, inelastic strains and stiffness degradation variables used in the definition of stress-strain behavior for tension and compression.

σ_t (MPa)	$\tilde{\varepsilon}_t^{in} \times 10^{-4}$ (-)	d_t (-)	σ_c (MPa)	$\tilde{\varepsilon}_c^{in} \times 10^{-3}$ (-)	d_c (-)
0	0	0	0	0	0
3.40	0	0	20.0	0	0
2.40	0.6	0.2727	40.0	0.3	0
1.60	1.3	0.5493	44.0	0.5	0
1.10	2.0	0.7317	47.6	0.8	0
0.90	2.3	0.7931	48.0	1.0	0
0.70	2.6	0.8478	47.8	1.2	0.0591
0.50	3.0	0.9000	47.0	1.5	0.1376
0.35	3.5	0.9375	40.0	2.3	0.3277
0.27	4.0	0.9569	20.0	4.0	0.6923
0.23	4.4	0.9663	16.0	4.5	0.7664
0.20	4.8	0.9730	11.0	5.5	0.8599
			8.0	7.0	0.9184
			7.0	8.0	0.9375

where $\tilde{\varepsilon}_t^{in}$ and $\tilde{\varepsilon}_c^{in}$ are the inelastic strains in tension and compression, respectively. Stresses and corresponding inelastic strains describing material behavior (Fig. 3) as well as stiffness degradation variables are given in Table 2.

The plastic flow is defined by the flow rule

$$\dot{\varepsilon}^{pl} = \dot{\lambda} \frac{\partial G(\bar{\sigma})}{\partial \bar{\sigma}} \tag{11}$$

where $\dot{\lambda}$ is the nonnegative plastic multiplier and G is the flow potential

$$G = \sqrt{(\epsilon \sigma_t^{\max} \tan\phi)^2} - \bar{p}\tan\phi. \tag{12}$$

where $\epsilon = 0.1$ is the flow potential eccentricity, $\sigma_t^{\max} = 3.4$ MPa is the uniaxial tensile stress at fracture (Table 2), $\phi = 31^\circ$ is the dilation angle in the p-q-plane (hydrostatic pressure - Mises equivalent stress) at high confining pressure and $\bar{p}$ is the effective hydrostatic pressure. Values for ϵ and ϕ represent typical values used for concrete [51]. The yield function $F \leq 0$ is

$$\begin{aligned} F(\bar{\sigma}, \tilde{\varepsilon}^{pl}) = & \frac{1}{1-\alpha}\left(\bar{q} - 3\alpha\bar{p} + \frac{1}{2}\left(\frac{\bar{\sigma}_c(\tilde{\varepsilon}_c^{pl})}{\bar{\sigma}_t(\tilde{\varepsilon}_t^{pl})}(1-\alpha) - (1+\alpha)\right)\right. \\ & \left. \cdot \left(|\hat{\bar{\sigma}}_{max}| + \hat{\bar{\sigma}}_{max}\right) - \frac{\gamma}{2}\left(|\hat{\bar{\sigma}}_{max}| - \hat{\bar{\sigma}}_{max}\right)\right) + \bar{\sigma}_c(\tilde{\varepsilon}_c^{pl}) \end{aligned} \tag{13}$$

where $\alpha = 0.12$ and $\gamma = 2.91$ are material constants based on reference [51], $\bar{q}$ is the Mises equivalent stress, $\bar{\sigma}_t$ and $\bar{\sigma}_c$ are the effective tensile and compressive cohesion stresses, respectively, and $\hat{\bar{\sigma}}_{max}$ is the maximum eigenvalue of the effective stress.

4. Simulation

In the simulations, the side of the subcube was 0.5 mm. An example of structure is shown in Fig. 4. The x_3-directional displacement was set to zero at the bottom of the sample and 2×10^{-3} mm displacement was applied into negative x_3-direction at the top of the sample, see Fig. 4. Displacements in the x_1- and x_2-directions were not restricted at any point in the subcube to ensure equal freedom in the x_1- and x_2-directions for each node. An example of the simulated stress-strain behavior of eight samples is shown in Fig. 5.

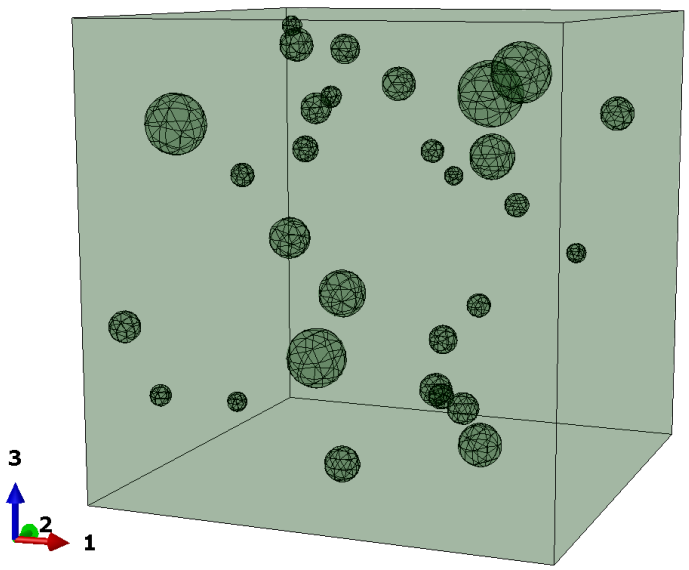

Figure 4: Example of subcube from Sample 2. Porous structure with 30 spherical pores and 1.00 % porosity. Bottom of the sample is defined by x_1-x_2-plane with $x_3 = 0$ mm and top of the sample by x_1-x_2-plane with $x_3 = 0.5$ mm. The size of the simulated samples is 0.5 mm $\times$ 0.5 mm $\times$ 0.5 mm.

The rigid body motions were prevented by a adding viscous forces term

$$F = cM^*v \tag{14}$$

where c is a damping factor, M^* is an artificial mass matrix calculated with unity density and v is the vector of nodal velocities to the equilibrium equations [46]. The example presented in Fig. 6 shows insensitivity of the results to the damping factor between 0.0001 1/s and 0.1 1/s; a constant damping factor of 0.01 1/s was used in all simulations.

In the simulations, the material experienced a reduction in stiffness and softening behavior reducing the convergence rate. To avoid too low con-

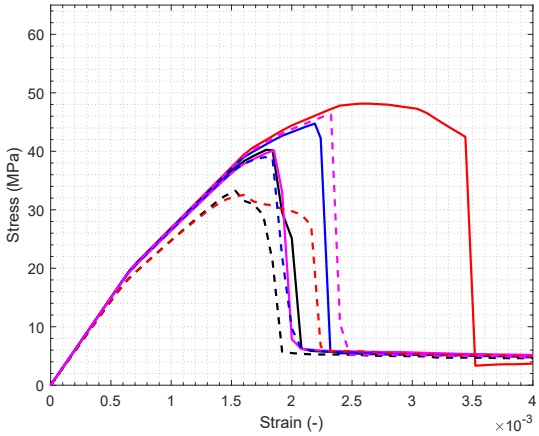

Figure 5: Simulated stress-strain behavior of eight samples.

vergence rate, viscoplastic regularization based on a generalization of the Duvaut-Lions regularization [52] was utilized. The regularized stress-strain relation

$$\sigma = (1 - d + \mu \dot{d}_v) D_0^{el} (\varepsilon - \varepsilon^{pl} + \mu \dot{\varepsilon}_v^{pl}) \tag{15}$$

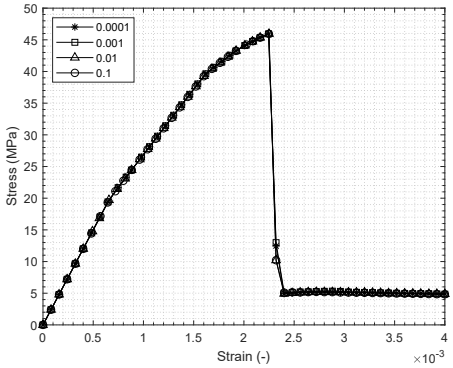

Figure 6: Effect of damping factor c (1/s) on the simulated results.

is obtained by adding a viscoplastic strain rate tensor $\dot{\varepsilon}_v^{pl}$ and viscous stiffness degradation rate $\dot{d}_v$ to Eq. (1). The intensity of regularization on the solution is determined by the value of the viscosity parameter μ. Fig. 7 shows the effect of the viscosity parameter on the simulated behavior for two subcubes. By making a compromise between the computation time and the effect of regularization, the value of the viscosity parameter used in the simulations was 0.0001 s.

Numerical solutions were obtained by finite element method (FEM) using Abaqus/Standard version 2018. The mesh was generated by free meshing technique with default mesh generation algorithm to create elements C3D10M [46]. Element C3D10M, a 10-node modified tetrahedron with hourglass control, was selected based on numerical testing emphasizing on the behavior of stress fields. During the simulations, excessive element distortion did not occur with the selected element type and boundary conditions. Excessive element distortion and automatic time incrementation scheme was

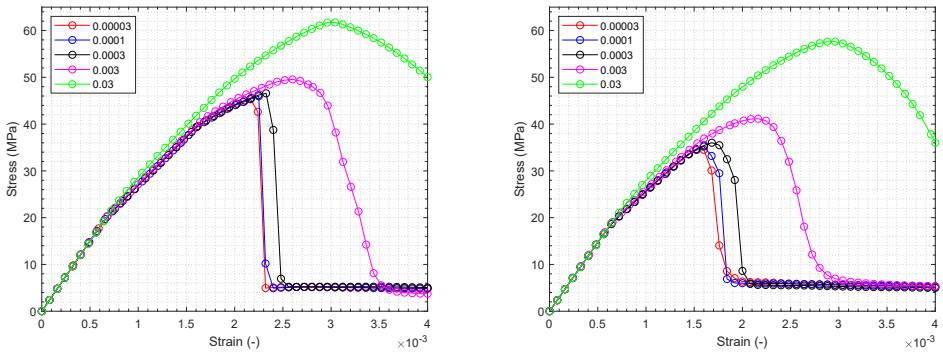

Figure 7: Effect of viscosity parameter μ (s) on the simulated results for $S1_\gamma$ (left) and $S2_\gamma$ (right).

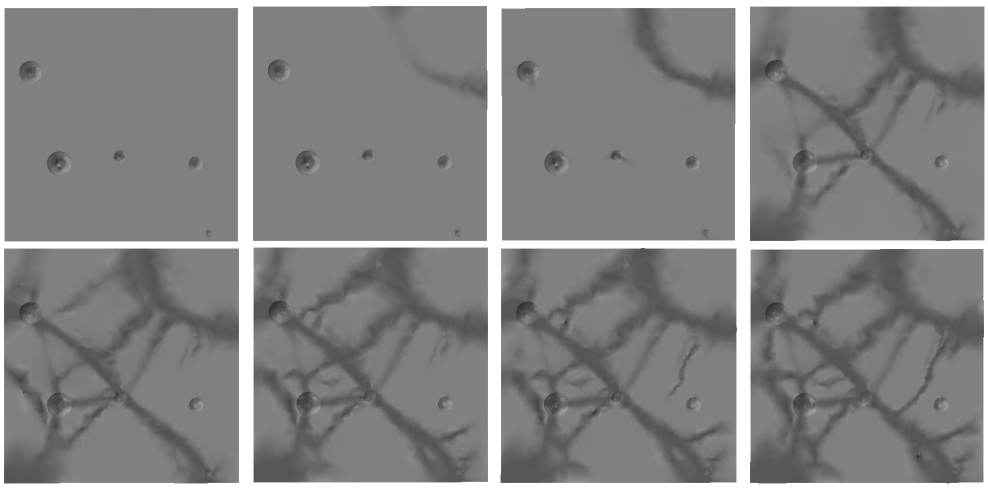

Figure 8: Stiffness degradation variable d from cross-section ($x_3 = 0.25$ mm) of $S2_\gamma$ during compression. Darker color correspond higher value of d. Compression in the top row from left to right: $8.0{\times}10^{-4}$ mm, $8.4{\times}10^{-4}$ mm, $8.8{\times}10^{-4}$ mm and $9.2{\times}10^{-4}$ mm. Compression in the bottom row from left to right: 9.6×10^{-4} mm, 1.4×10^{-3} mm, 1.6×10^{-3} mm and 2.0×10^{-3} mm. The size of the sample is 0.5 mm $\times$ 0.5 mm $\times$ 0.5 mm.

controlled by Abaqus [46]. An example of damage behavior is shown in Fig. 8 and the porous structure of the corresponding sample in Fig. 9. Due to the behavior of a structure including softening of the material and damage behavior, mesh density affects on the numerical solution [53, 54]. Fig. 10 shows that a denser mesh causes the specimen to lose its load carrying capacity with a lower load. However, the compressive strength of low and high porosity subcubes appears to behave similarly as a function of mesh density. To reasonable the computation time, a seed of 0.050 mm was chosen to be used in the mesh generation. Fig. 11 represents how the results shown in Fig. 10 are located among the simulated results for all samples.

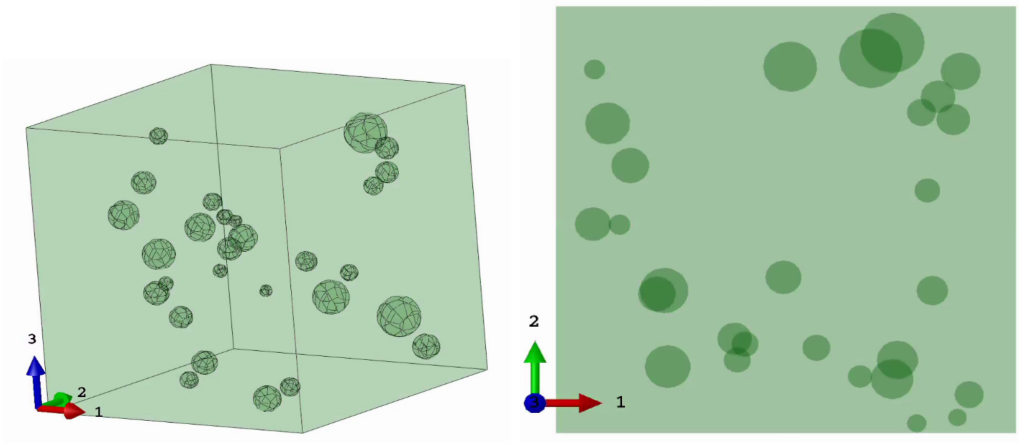

Figure 9: Porous structure of a sample which simulated damage behavior is shown in Fig. 8: 3D representation of the sample (left) and projection into a plane perpendicular to the direction of compression (right). The sample size is 0.5 mm × 0.5 mm × 0.5 mm.

5. Results

The simulation procedure was performed on 128 subcube specimens. The measured pore distributions of Sample 1 and Sample 2 were the basis for two

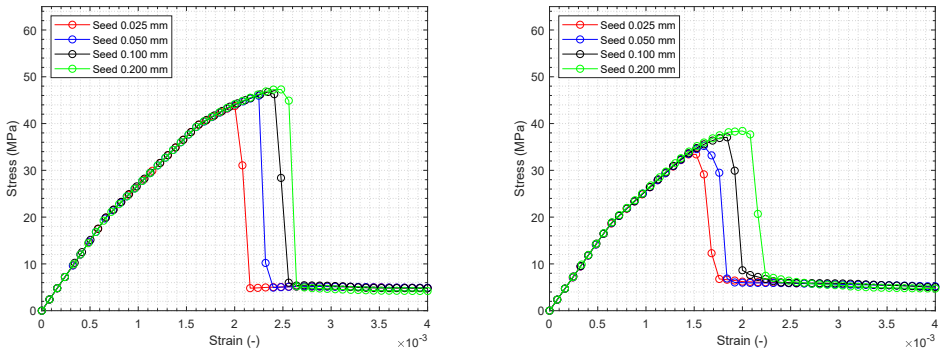

Figure 10: Effect of mesh density on the simulated results for $S1_\gamma$ (left) and $S2_\gamma$ (right).

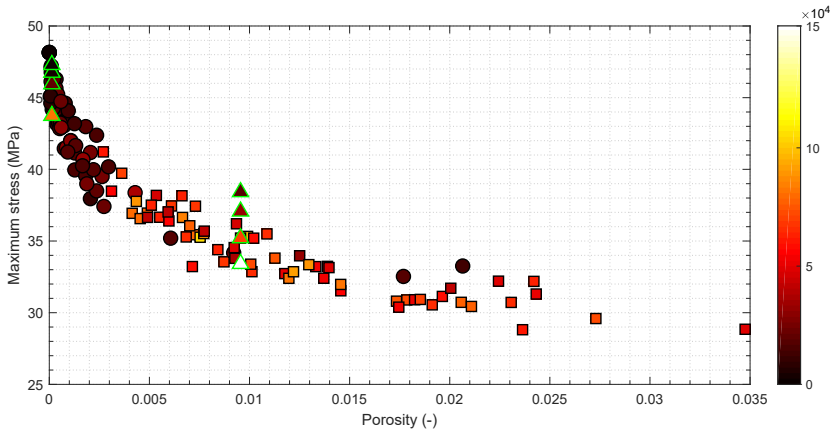

Figure 11: Simulated maximum stress as a function of porosity and the effect of the mesh density. Circles and squares are used for samples based on Sample 1 and Sample 2, respectively. Color of the markers describes the number of elements in the sample and triangles with green edges represent the mesh density tests in Fig. 10.

sets of structures, S1 and S2; 64 subcube specimens were taken from each. The simulated maximum stresses as a function of porosity and number of pores in the subcube specimens are presented in Fig. 12 (see also Tables A.5 and A.6 (Appendix)). The number of pores divides the subcubes into two separate groups; the number of pores in S1 varies between 0 and 8 and in S2 between 14 and 35. However, the properties of S1 and S2 intersect in terms of porosity and compressive strength, as even a single large pore at the volume of interest significantly increases porosity, see Fig. 12.

Several general types of functions developed to model the relationship between strength σ^{max} and porosity p of engineering materials have been commonly utilized in the field of cement-based material research, e.g.,

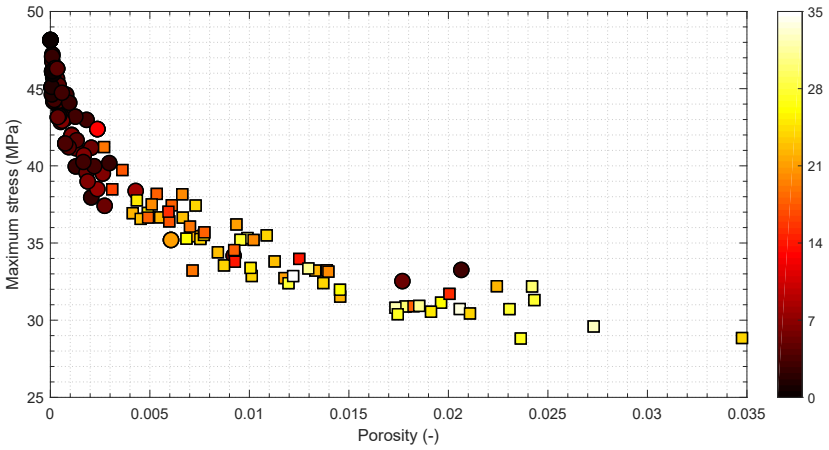

Figure 12: Simulated maximum stress as a function of porosity. Subcubes from Sample 1 are marked with circles and from Sample 2 with squares. Color of the markers describes the number of pores in a sample.

$$\sigma^{max} = \sigma_0(1-p)^{k_1} \qquad \text{(Balshin [11])} \tag{16}$$

$$\sigma^{max} = \sigma_0 e^{-k_2 p} \qquad \text{(Ryshkewitch [12])} \tag{17}$$

$$\sigma^{max} = k_3 \ln\left(\frac{p_0}{p}\right) \qquad \text{(Schiller [13])} \tag{18}$$

$$\sigma^{max} = \sigma_0 - k_4 p \qquad \text{(Hasselman [14])} \tag{19}$$

where σ_0 is the strength at zero porosity, k_i are constants and p_0 is the porosity at zero strength. Atzeni et al. [10] proposed a formula for hardened cement pastes in which, in addition to porosity p, the strength is related to mean distribution pore radius r_m

$$\sigma^{max} = k_5 \sigma_0 \frac{1-p}{\sqrt{r_m}}. \tag{20}$$

In this study, a volume weighted mean radius is used for r_m as

$$r_m = \frac{\sum V_n r_n}{\sum V_n} \tag{21}$$

where V_n is the volume and r_n is the radius of the pore n. Li et al. [15] used a simplified center pore model to derive an analytical solution for compressive strength of concrete

$$\sigma^{max} = \sigma_0 \frac{(1-c)^2}{5c+1} \tag{22}$$

where c is defined as

$$c = \frac{r_p^2}{r_V^2} = p^{2/3}. \tag{23}$$

In Eq. (23) r_p is the volume equivalent sphere radius of the sum of the pore volumes and r_V is the volume equivalent sphere radius of the subcube (V_γ = 0.5 mm $\times$ 0.5 mm $\times$ 0.5 mm).

Fig. 13 shows the least-squares fits of the above mentioned six strength-porosity relation models to the simulated data. The fittings have been applied to the entire data (S1+S2) as well as separately to the sample sets S1 and S2. Root-mean-square deviation (RMSD) is used as a measure of goodness of fit. Regardless of the data set to which the fittings are made (S1, S2 or S1+S2), deviations are always calculated using the entire data set (S1+S2). The fitting parameters and deviations are presented in Table 3.

The formulas of Balshin, Ryshkewitch, and Hasselman (Eqs. (16), (17) and (19)) each contain two fitting parameters, σ_0 and k_i. Based on the

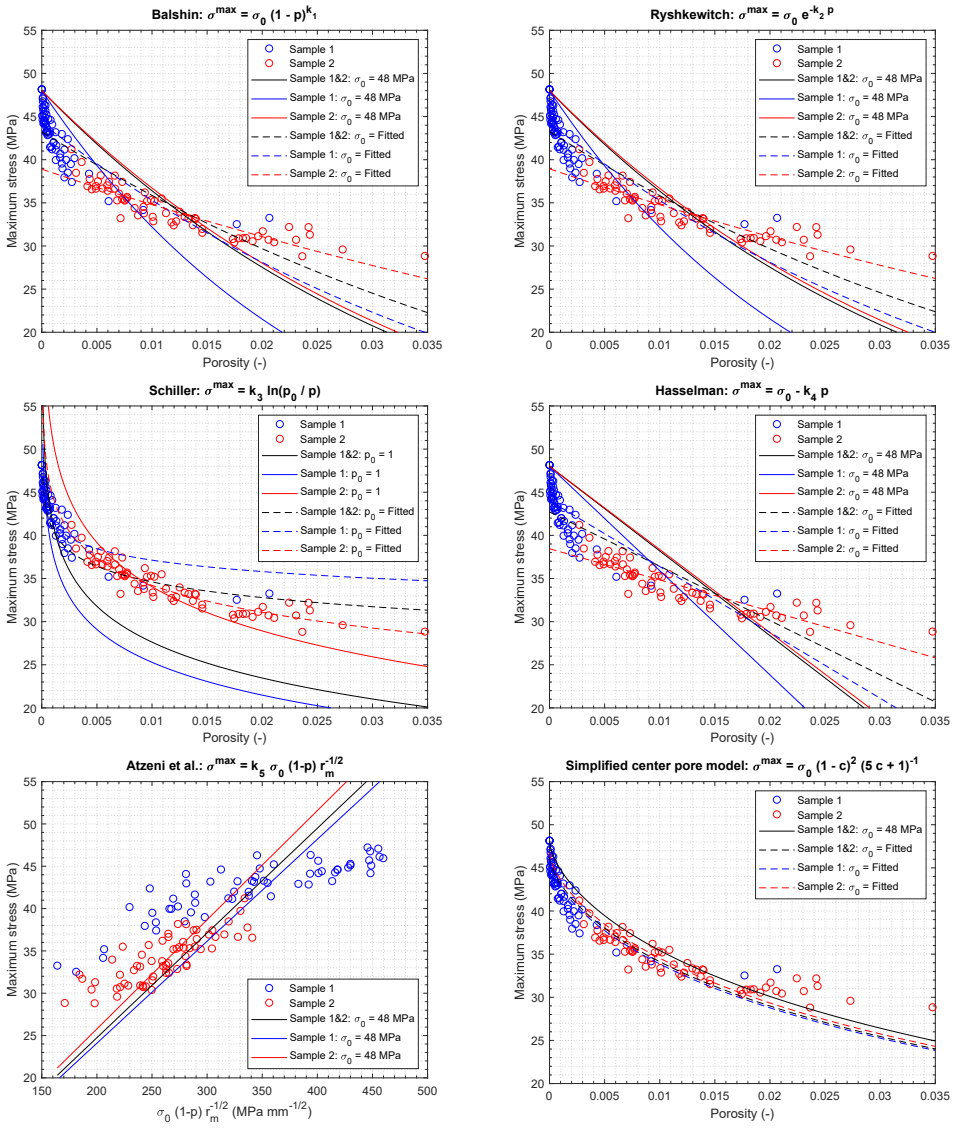

Figure 13: Eqs. (16)-(20) and (22) fitted to the simulated results. Fittings are done for result data concerning Sample 1 (blue), Sample 2 (red) and both samples (blue and red: black line) by fitting with all parameters free (dashed line) and with one parameter fixed (solid line). Parameters are given in Table 3.

Table 3: Fitted parameters and root-mean-square deviation (RMSD) for Eqs. (16)-(20) and (22). Fixed parameters are given in bold font and fittings are done for simulated results concerning Sample 1, Sample 2 and both samples.

Sample	1&2	1	2	1&2	1	2
Balshin [11]						
σ_0 (MPa)	**48**	**48**	**48**	43.245	44.248	38.902
k_1 (-)	27.531	39.722	26.672	18.626	22.473	11.105
p_0 (-)	1	1	1	1	1	1
RMSD (MPa)	3.933	5.063	3.941	2.254	2.430	3.771
Ryshkewitch [12]						
σ_0 (MPa)	**48**	**48**	**48**	43.267	44.258	38.943
k_2 (-)	27.781	40.067	26.914	18.841	22.707	11.282
p_0 (-)	∞	∞	∞	∞	∞	∞
RMSD (MPa)	3.910	5.046	3.918	2.240	2.415	3.749
Schiller [13]						
k_3 (MPa)	5.998	5.491	7.394	2.617	1.907	4.506
p_0 (-)	**1**	**1**	**1**	5.536e3	2.847e6	19.810
RMSD (MPa)	7.060	7.761	11.333	1.753	2.678	4.672
Hasselman [14]						
σ_0 (MPa)	**48**	**48**	**48**	42.715	44.013	38.448
k_4 (MPa)	0.981e3	1.209e3	0.964e3	0.629e3	0.763e3	0.361e3
p_0 (-)	0.049	0.040	0.050	0.068	0.058	0.107
RMSD (MPa)	4.637	5.181	4.641	2.515	2.734	4.030
Atzeni et al. [10]						
σ_0 (MPa)	**48**	**48**	**48**	-	-	-
k_5 ($mm^{1/2}$)	0.124	0.121	0.129	-	-	-
p_0 (-)	1	1	1	-	-	-
RMSD (MPa)	5.404	5.495	5.636	-	-	-
Simplified center pore model [15]						
σ_0 (MPa)	**48**	-	-	46.236	45.888	46.795
p_0 (-)	1	1	1	1	1	1
RMSD (MPa)	2.181	-	-	1.604	1.630	1.671

material model used in the simulations, the compressive strength at zero porosity is $\sigma_0 = 48$ MPa. Eqs. (16), (17) and (19) are fitted using first the

fixed value for $\sigma_0 = 48$ MPa and then the free parameters for σ_0 and k_i. When fixed σ_0 is used, the RMSDs are high, but the deviations decreases when models are fitted with free parameters. At low porosity values the Balshin, Ryshkewitch and Hasselman models equal. This can be easily seen by Taylor expanding the Balshin Eq. (16) and the Ryshkewitch Eq. (17) models as function of porosity and by taking only the two leading terms for low porosity. This equivalency at low porosity values is also observed when fitting the models in the simulation results. At very low porosities, the curves do not bend steeply enough, underestimating the strength at the zero porosity, and the fits of Eqs. (16), (17) and (19) extrapolate nearly identical values to σ_0 (Table 3). Porosity at zero strength is one for Balshin and infinity for Ryskewitch based on the type of equations. The Hasselman's model extrapolates low values to the fitting variable p_0, ranging from 4.0 % to 10.7 % depending on data set and the fitting approach.

Schiller's equation (Eq. (18)) goes to infinity at zero porosity. To include subcubes with zero porosity in the fittings of Schiller, the porosity is set to $p = 10^{-5}$ for those subcubes. The values of the fitting parameter p_0 are unrealistically high. The Schillers's models were also fitted using a fixed porosity $p_0 = 1$, but the deviations increased even more. In the Atzeni's model (Eq. (20)), in addition to the porosity p, the variable r_m describing the pore distribution is included. However, ideal linearization is not achieved and the approach does not reduce scattering of data points around the strength-porosity relationship curve.

The solution of Li's formula (Eq. (22)) can be directly calculated when σ_0 is know, but by fitting the equation an estimate for σ_0 is also provided. The

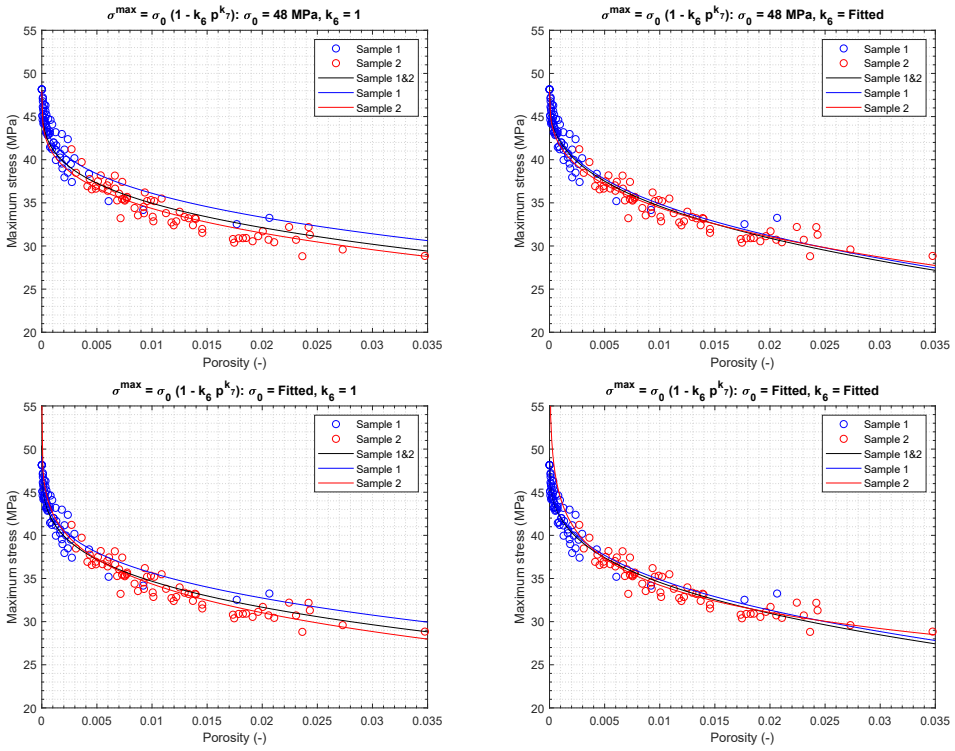

Figure 14: Eq. (24) fitted to the simulated results with different combinations of fixed and free state of parameters σ_0 and k_5. Fittings are done for result data concerning Sample 1 (blue), Sample 2 (red) and both samples (blue and red: black line). Parameters and approximated σ_0 and p_0 are given in Table 4.

fits are fairly independent of data set and the lowest RMSDs were achieved when compared to the deviations observed with other formulas studied. The values of σ_0 are only slightly underestimated by fitting. The Li's model follows quite well the data at low porosity, but differs more with increasing porosity.

It appeared in this study that a simple power law function p^{k_7} could provided a good alternative to linearize the relationship. By using $1 - p^{k_7}$ to

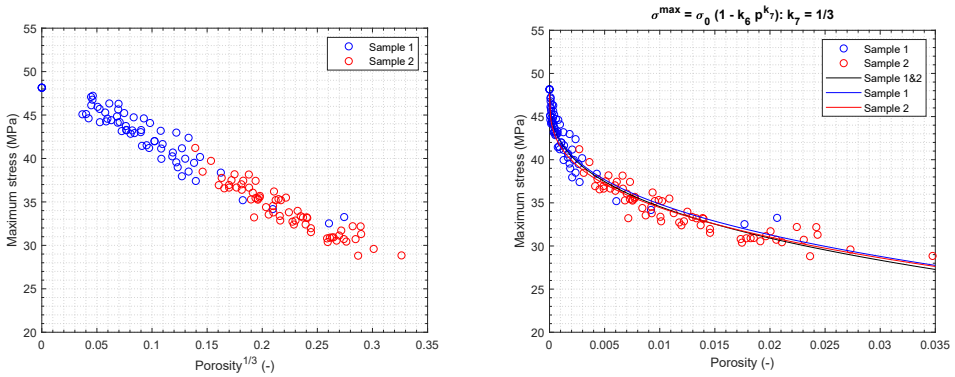

Figure 15: Linearized data (left) and Eq. (24) fitted with $k_7 = 1/3$ (right). Fittings are done for results concerning Sample 1 (blue), Sample 2 (red) and both samples (blue and red: black line). Parameters and approximated σ_0 and p_0 are given in Table 4.

change from a negative correlation to a positive correlation and constants k_6 and σ_0 for scaling, the model takes a form

$$\sigma^{max} = \sigma_0(1 - k_6 p^{k_7}) \tag{24}$$

where k_6 and k_7 are the fitting parameters. In total, the model contains three fitting parameters, which can make the fitting unstable and extrapolation of σ_0 and p_0 unreliable. If σ_0 is fixed to 48 MPa and k_6 to 1, the equation passes through two points $(p, \sigma) = (0, 48)$ and $(1, 0)$, and then the constant k_7 defining the shape of the function is only fitting parameter. The results of these fittings are presented in the upper-left in Fig. 14. The upper-right figure shows the fitting results with free k_6, in which case the estimates for p_0 are derived, see Table 4. For both of these approaches, the RMSDs are low and fitting is quite insensitive to data set selection. Estimation of σ_0 can be derived with the fixed $k_6 = 1$ or with all three parameters free, see

bottom-left and bottom-right in Fig. 14. The fittings of the data set S2 expose the sensitivity of determining σ_0 and p_0 by extrapolation. However, the behavior can be stabilized by using fixed exponent $k_7 = 1/3$. The degree of linearization is illustrated in the left in Fig. 15 and corresponding fits are presented in the right in Fig. 15. The deviations are low regardless of the data set in fitting and estimates for σ_0 and p_0 are in reasonable range, see Table 4. The use of exponent value 1/3 can be interpreted as a change of variable substituting the porosity by ratio of radius of volume equivalent spheres or ratio of side lengths of volume equivalent cubes, i.e., $p^{1/3} = r_p/r_V$ or $p^{1/3} = l_p/l_V$ where r_p and r_V are as in Eq. (23), l_p is the volume equivalent cube side length of the sum of the pore volumes and l_V is the volume equivalent cube side length of the subcube (0.5 mm). Now Eq. (24) can be written in the form $\sigma^{max} = \sigma_0(1 - k_6\xi)$, where ξ is defined as the void length ratio $\xi = p^{1/3}$. σ_0 defines the maximum stress at zero porosity, while single fitting parameter k_6 defines porosity at zero maximum stress in the form $p_0 = k_6^{-1/3}$. The model assumes a simple linear decrease of maximum strength as a function of increasing void length ratio, ξ, between points $(\xi, \sigma) = (0, \sigma_0)$ and $(\xi, \sigma) = (1/k_6, 0)$.

6. Discussions

The simulations were performed on CSC's (the Finnish IT center for science) new supercomputer Puhti. For one standard sample simulation, a wall clock time of 36 hours was set aside, during which time all samples exceeded the maximum stress point. The computation time required to simulate the entire compressible distance was considerably longer, varying from several

Table 4: Parameters and root-mean-square deviation (RMSD) for Eq. (24) fits. Fixed parameters are given in bold font and fittings are done for simulated results concerning Sample 1, Sample 2 and both samples.

Sample	σ_0	k_6	k_7	p_0	RMSD (MPa)
1&2	**48**	**1**	0.283	1.000	1.375
1	**48**	**1**	0.303	1.000	1.707
2	**48**	**1**	0.273	1.000	1.477
1&2	**48**	1.416	0.353	0.373	1.103
1	**48**	1.419	0.358	0.376	1.126
2	**48**	1.235	0.320	0.517	1.173
1&2	50.410	**1**	0.253	1.000	1.199
1	49.212	**1**	0.280	1.000	1.441
2	55.996	**1**	0.207	1.000	1.850
1&2	48.886	1.292	0.322	0.451	1.084
1	48.608	1.298	0.331	0.455	1.114
2	209.186	0.942	0.026	10.176	28.533
1&2	48.629	1.342	**1/3**	0.413	1.087
1	48.572	1.311	**1/3**	0.444	1.112
2	47.629	1.284	**1/3**	0.472	1.190

days to two weeks. The wall clock time needed for the simulations was decreased by paralleling the computation, see Fig. 16. In the simulations, the convergence rate strongly depends on the intensity of regularization and, to a lesser extent, the mesh density. Higher convergence rate is easily achieved by increasing the intensity of regularization. However, with too high intensity the regularization begins to dominate the solution. A denser mesh may also increase the convergence rate at that price that the computation time used to solve set of equations increases dramatically. Naturally, the sample size

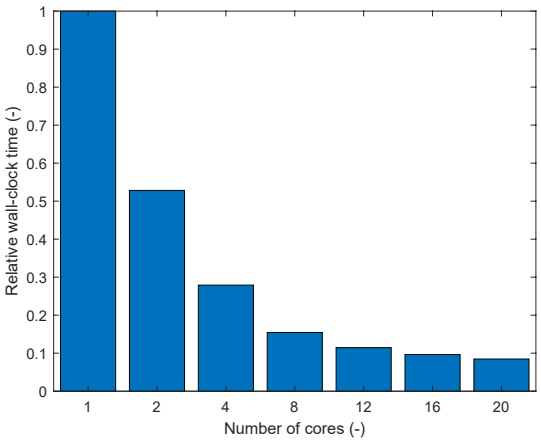

Figure 16: Effect of parallelization on wall clock time.

also affects the size of the set of equations to be solved.

The X-ray tomography image pixel size (here 5 μm), resolution and noise in the images restricts the size of pore structures which can be reliably distinguished from the images. Also, the image processing and analysis, such as filtering, thresholding and watershed, affects the porosity results obtained from the images. With the present imaging set-up and analysis methods, discussed in detail in Section 2.2, the results obtained for pore-like structures less than 50 voxels are considered unreliable, which also indicates that the capillary pores cannot be investigated in the current study. To capture smaller pore structures, one should use larger geometrical magnification in imaging or different higher resolution tomography scanner and longer image exposure times. Also, different, more sophisticated, filtering and thresholding methods might provide more insight for pore structures. To further estimate and reduce the perceptible uncertainty in the pore number distributions one could

try to validly combine the current watershed results, utilizing 18-connected neighborhood, with another 26-connected neighborhood watershed analysis results. In related analysis it was observed that the total number of pores can be clearly larger when using 26-connected neighborhood in watershed analysis. Particularly number of smaller pores got increased. Part of this increase is justified i.e. there are more connected small pores than indicated by 18-connected analysis. But part of the increase is due to over-segmentation of some pore structures e.g. some non-spherical voids, like some cracks, get over-segmented. Thus, further investigation and possible combination of 18- and 26-connected results would be reasonable. The use of seed images in the watershed analysis could improve the watershed results also. These are subjects for possible further studies.

The presented simulation approach is based on compromises related to the above issues, while the measurement method limits the category of pores considered. The number of pores in one simulation subcube is small and they can be categorized as macroscale pores corresponding air voids. The choice of spherical pores, of course, affects the simulation results, but serves as a good estimate for the air pores on which research has focused. The base of the statistics was established by simulating 128 subcubes generated by sampling from pore structures of two mortar: Sample 1 and Sample 2. Sample 1 and Sample 2 differ in the porosity distribution; both structures results in groups of 64 subcubes that differ in variations of porosity, pore distribution and pore placement. However, the material model used in the simulations of all subcubes is the same so that it is possible to study the effect on strength due to porosity and pore size distribution alone. Thus, a general trend can

be observed as well as scattering around it for the simulated compressive strength-porosity relation as can be seen from Fig. 12.

The nonlinear general trend of decreasing maximum stress with increasing porosity was successfully linearized using cubic root of porosity, i.e., $p^{1/3}$. Interestingly, the physical meaning of $p^{1/3}$ can be interpreted as the ratio of volume equivalent sphere radii or volume equivalent cube sides of void and total volume, i.e., the void length ratio ξ. Decrease in maximum stress appears to be linear as a function of ξ . Whether this is fundamental behavior or associated to spherical shape of pores or other material model issues in simulations, is a question for further research. Exemplary fittings of that model to a few measured data sets are shown in Fig. 17. Despite the diversity of materials and methods of preparation between and within data sets and differences in measurement techniques, the formula Eq. (24) appears to model the data in the examples considered reasonably well. The model also gives estimates for both parameters σ_0 and p_0. Uncertainty in extrapolating values significantly beyond the data observed is obvious. Approximated pressure at zero strength obtains reasonable values, $p_0 < 1$. No conclusions can be drawn about the accuracy of σ_0 approximations due to the lack of low porosity data.

No clear correlation was found between scattering around trend and parameters related to pore size distribution, such as number of pores or volume-weighted mean pore size. In general, the effect of pore size distribution remained unresolved; the small number of pores in each individual subcube caused that a statistical analysis of the porosity distribution of the subcube could not be reasonably performed. The placement and clustering of single pores may explain this variation, but appeared difficult to study. The causes

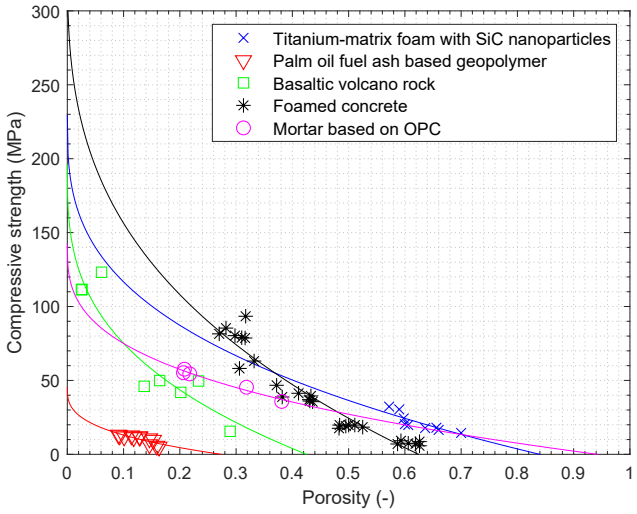

Figure 17: Eq. (24) fitted to the published data: Titanium-matrix foam [55], geopolymer [56], basaltic volcano rock [57], foamed concrete [58] and mortar [59].

of scattering around the trend line in terms of maximum stress and porosity remains unresolved in this study.

7. Conclusions

A large number of simulations were performed to reveal the compressive strength-porosity relation for quasi-brittle material at low porosity region from zero to 3.5 %. 128 stochastic structures that included only variability due to porosity, pore distribution and pore placement were generated for simulations based on measured distributions. Practical factors related to material, measurement method and simulation approach limited the porosity, the side length and the number of pores of a single cube used in simulations. The use of X-ray microtomography in pore distribution measurements di-

rected the focus of this study towards air pores and established the use of spherical pores in the simulations. The finite element method used causes limitations on, for example, the size of the structure and number of pores due to computational time. However, the generation of porous structure is practical even with a commercial program by using scripting interface. The resulting simulated strength-porosity relationship included a clear trend and some scattering around it. The relationship was convincingly linearized with cubic root of porosity ($p^{1/3}$), suggesting that the ratio of volume equivalent sphere radii or volume equivalent cube sides of void and total volume correlate linearly to compressive strength. There was no simple explanation for scattering around strength-porosity trend. The approach presented in this paper made it possible to study the effect of porosity on compressive strength without disturbances due to material property variations.

Acknowledgements

This research was supported by Regional Council of Central Finland and European Regional Development Fund (ERDF) - Sustainable Bioresidual Concrete. Simulations were performed by CSC's (the Finnish IT center for science) Puhti supercomputer and commercial software Abaqus which was licensed to CSC. Samples were prepared in the concrete testing laboratory of JAMK University of Applied Science.

Appendix A.

Data tables of subcubes.

Table A.5: Sample 1: Number of pores with radius r (μm), mean of radius r (μm), standard deviation (SD) of radius r (μm), porosity p (%) and simulated maximum stress σ^{max} (MPa).

Sample	$10 \leq r < 15$ μm	$15 \leq r < 20$ μm	$20 \leq r < 25$ μm	$25 \leq r < 30$ μm	$30 \leq r < 50$ μm	$50 \leq r < 250$ μm	Mean r (μm)	SD r (μm)	p (%)	σ^{max} (MPa)	Sample	$10 \leq r < 15$ μm	$15 \leq r < 20$ μm	$20 \leq r < 25$ μm	$25 \leq r < 30$ μm	$30 \leq r < 50$ μm	$50 \leq r < 250$ μm	Mean r (μm)	SD r (μm)	p (%)	σ^{max} (MPa)
1	3	0	0	0	0	0	11.3	1.0	0.015	44.18	33	1	3	0	0	0	0	17.1	3.2	0.072	43.03
2	3	0	0	1	1	0	18.3	10.0	0.182	39.56	34	2	0	1	0	0	0	14.8	6.1	0.044	43.74
3	5	0	0	0	0	0	12.3	1.3	0.032	44.84	35	0	0	0	0	0	0	0.0	0.0	0.000	48.15
4	3	2	0	0	0	0	14.4	1.8	0.052	42.85	36	3	0	0	0	0	0	12.3	0.9	0.019	45.29
5	1	0	0	1	1	0	24.9	11.4	0.220	39.97	37	0	1	1	0	1	0	24.6	7.9	0.182	42.98
6	1	0	0	0	0	0	13.2	0.0	0.008	44.62	38	1	0	0	0	0	0	11.4	0.0	0.005	45.09
7	4	2	0	0	0	0	13.7	3.3	0.059	42.92	39	3	0	0	0	0	0	12.6	1.8	0.021	44.58
8	2	1	0	0	0	0	12.2	2.6	0.020	44.27	40	2	0	1	0	0	0	15.4	5.0	0.045	43.29
9	4	1	0	0	1	0	17.2	11.9	0.264	39.50	41	2	1	0	0	1	0	19.5	13.8	0.236	42.38
10	1	0	0	0	1	0	22.6	14.8	0.128	39.96	42	2	0	0	0	0	0	11.0	0.3	0.009	46.13
11	3	0	1	0	1	0	20.0	12.0	0.273	37.41	43	3	0	0	0	0	0	10.9	0.3	0.013	45.95
12	2	1	0	0	1	1	28.4	20.1	0.921	34.18	44	0	2	0	0	0	1	29.8	22.3	0.606	35.20
13	4	1	1	0	0	0	16.3	4.8	0.107	41.98	45	3	1	1	0	0	0	15.7	3.9	0.075	41.45
14	2	0	0	0	0	0	11.2	1.4	0.010	46.77	46	1	0	1	0	0	0	16.8	6.1	0.038	43.15
15	5	0	0	1	1	0	17.9	8.9	0.236	38.50	47	1	0	1	0	0	0	15.8	6.8	0.034	46.30
16	5	0	0	2	1	0	19.8	11.6	0.429	38.37	48	6	0	0	0	0	0	12.9	1.8	0.045	43.25
17	1	0	1	0	1	0	22.4	10.5	0.166	40.25	49	5	0	1	0	0	0	14.6	5.3	0.086	41.52
18	0	0	0	0	0	0	0.0	0.0	0.000	48.15	50	0	0	0	0	0	0	0.0	0.0	0.000	48.15
19	1	1	1	0	0	0	17.4	3.7	0.058	44.74	51	2	1	1	0	1	0	18.6	10.6	0.206	41.18
20	1	0	0	0	1	0	28.4	22.3	0.296	40.18	52	3	0	0	0	0	0	11.2	1.4	0.014	45.70
21	0	1	1	0	0	1	42.3	36.3	2.065	33.26	53	2	0	1	0	0	0	15.6	7.1	0.055	43.23
22	1	1	1	0	1	1	34.1	26.1	1.769	32.53	54	4	1	0	0	1	0	17.1	8.1	0.168	40.69
23	2	2	1	0	1	0	18.6	7.6	0.187	38.99	55	3	1	0	0	0	0	12.8	3.4	0.033	44.12
24	2	1	0	0	0	0	12.3	3.9	0.023	46.33	56	2	0	0	1	0	0	18.0	7.2	0.079	44.61
25	3	0	1	0	0	0	13.2	5.0	0.042	45.23	57	3	0	2	0	0	0	16.6	6.7	0.107	42.01
26	2	0	0	0	0	0	11.0	1.1	0.009	47.08	58	3	0	0	0	0	0	13.2	2.6	0.025	44.41
27	2	0	0	0	0	0	11.3	1.6	0.010	47.22	59	2	0	2	1	0	0	18.2	6.0	0.127	41.14
28	1	0	0	0	1	0	20.4	13.6	0.095	44.08	60	3	1	0	0	0	0	13.6	2.1	0.035	44.19
29	1	2	0	1	0	0	17.2	6.5	0.092	41.21	61	0	1	1	1	0	0	22.2	5.7	0.126	43.19
30	0	0	0	0	0	0	0.0	0.0	0.000	48.15	62	1	0	0	0	1	0	24.6	20.6	0.205	37.95
31	2	1	0	0	1	0	18.1	9.2	0.132	41.66	63	3	1	0	0	0	0	13.2	2.5	0.033	45.65
32	1	0	0	0	0	0	12.5	0.0	0.006	45.12	64	0	1	2	0	0	0	19.1	2.7	0.073	43.27

Table A.6: Sample 2: Number of pores with radius r (μm), mean of radius r (μm), standard deviation (SD) of radius r (μm), porosity p (%) and simulated maximum stress σ^{max} (MPa).

Sample	$10 \leq r < 15$ μm	$15 \leq r < 20$ μm	$20 \leq r < 25$ μm	$25 \leq r < 30$ μm	$30 \leq r < 50$ μm	$50 \leq r < 250$ μm	Mean r (μm)	SD r (μm)	p (%)	σ^{max} (MPa)	Sample	$10 \leq r < 15$ μm	$15 \leq r < 20$ μm	$20 \leq r < 25$ μm	$25 \leq r < 30$ μm	$30 \leq r < 50$ μm	$50 \leq r < 250$ μm	Mean r (μm)	SD r (μm)	p (%)	σ^{max} (MPa)
1	5	6	10	1	0	0	18.6	4.6	0.552	36.66	33	10	8	6	1	4	1	20.8	10.8	1.785	30.89
2	10	7	8	2	3	1	21.1	10.5	1.853	30.93	34	6	2	6	4	4	0	22.6	9.6	1.331	33.21
3	11	8	3	6	5	1	21.7	10.1	2.057	30.72	35	6	6	0	0	2	1	22.0	17.5	2.005	31.70
4	11	8	1	3	3	1	20.9	13.5	2.364	28.81	36	11	7	3	1	2	0	17.8	7.6	0.753	35.26
5	13	7	4	4	3	1	20.4	10.1	1.734	30.80	37	8	3	2	2	3	1	22.3	11.8	1.389	33.23
6	8	9	6	3	2	0	19.6	6.6	0.955	35.21	38	7	9	4	3	1	0	19.1	6.0	0.730	37.43
7	4	7	2	3	1	0	19.6	7.0	0.598	36.40	39	12	10	3	1	4	0	18.4	7.6	0.990	35.32
8	11	8	4	1	2	0	17.8	6.2	0.684	35.28	40	10	6	2	0	2	1	19.3	11.3	1.176	32.73
9	7	4	3	3	1	0	18.8	7.6	0.610	37.44	41	8	8	3	3	2	2	21.8	12.1	1.963	31.14
10	12	7	2	0	1	0	15.3	6.0	0.414	36.93	42	17	3	1	4	0	0	15.9	5.9	0.490	36.95
11	11	7	3	0	3	0	18.0	8.7	0.873	33.55	43	9	6	2	3	2	1	20.0	9.5	1.127	33.81
12	4	7	6	0	5	0	22.8	10.2	1.456	31.53	44	9	5	2	1	1	0	17.3	7.6	0.535	38.18
13	9	2	2	3	3	1	22.0	11.7	1.397	33.15	45	2	4	2	2	4	0	23.8	9.2	0.927	33.79
14	13	7	1	1	4	2	21.7	13.2	2.307	30.72	46	12	4	3	1	2	0	18.0	7.9	0.729	35.44
15	8	6	4	2	3	1	22.9	16.7	3.475	28.84	47	14	5	3	1	2	0	17.4	7.8	0.753	35.38
16	13	5	4	1	0	1	17.7	10.0	1.087	35.50	48	10	9	4	2	7	1	22.6	12.4	2.730	29.59
17	8	6	0	3	2	0	18.8	8.4	0.702	36.06	49	11	3	0	2	0	0	16.0	5.7	0.311	38.48
18	6	8	2	0	2	0	18.6	9.3	0.774	35.69	50	15	9	6	0	5	0	18.3	8.1	1.220	32.86
19	8	5	6	4	0	2	21.5	12.3	1.913	30.55	51	8	5	4	2	2	0	19.8	8.9	0.935	36.20
20	10	3	7	1	6	0	22.3	10.6	1.746	30.39	52	8	6	5	3	2	0	19.7	8.4	1.012	32.86
21	9	4	7	1	4	1	21.3	9.7	1.455	31.97	53	4	2	5	0	2	1	22.8	12.9	1.250	33.97
22	11	8	3	2	5	1	21.8	12.9	2.420	32.18	54	5	3	3	1	4	2	25.3	13.0	1.824	30.90
23	10	5	5	1	2	1	20.5	13.6	2.108	30.44	55	4	7	5	3	5	0	22.7	8.6	1.371	32.40
24	10	10	6	2	3	0	19.6	8.4	1.296	33.35	56	9	5	4	2	1	1	20.8	14.5	2.244	32.20
25	11	2	1	0	3	1	18.9	11.0	0.923	34.54	57	7	6	2	2	0	0	17.2	5.0	0.362	39.73
26	14	4	0	0	1	0	14.7	4.6	0.270	41.22	58	12	5	5	1	4	1	20.9	13.4	2.432	31.30
27	7	10	5	1	0	0	17.3	3.8	0.454	36.56	59	4	9	1	1	5	0	21.7	8.5	1.021	35.20
28	7	6	1	4	0	0	18.1	6.3	0.491	36.65	60	14	2	6	0	1	0	16.6	7.9	0.665	36.65
29	7	9	4	3	1	0	18.8	6.9	0.771	35.52	61	11	6	6	2	3	0	19.6	8.7	1.197	32.40
30	6	4	2	2	1	0	18.8	8.9	0.593	37.03	62	13	7	4	1	0	0	16.0	4.6	0.435	37.76
31	12	3	1	1	3	0	18.0	8.3	0.663	38.16	63	11	5	2	1	1	0	17.1	6.4	0.510	37.50
32	5	7	9	2	2	0	20.6	7.0	1.006	33.38	64	8	4	3	1	3	0	19.2	8.3	0.715	33.22

References

[1] I. Odler, M. Rößler, Investigations on the relationship between porosity, structure and strength of hydrated Portland cement pastes. II. Effect of pore structure and of degree of hydration, Cement and Concrete Research 15 (3) (1985) 401 – 410.

[2] C. Shi, Strength, pore structure and permeability of alkali-activated slag mortars, Cement and Concrete Research 26 (12) (1996) 1789 – 1799.

[3] B. Zhang, Relationship between pore structure and mechanical properties of ordinary concrete under bending fatigue, Cement and Concrete Research 28 (5) (1998) 699 – 711.

[4] L. Jiang, Y. Guan, Pore structure and its effect on strength of high-volume fly ash paste, Cement and Concrete Research 29 (4) (1999) 631 – 633.

[5] Y.N. Chan, X. Luo, W. Sun, Compressive strength and pore structure of high-performance concrete after exposure to high temperature up to 800°C, Cement and Concrete Research 30 (2) (2000) 247 – 251.

[6] C.S. Poon, S.C. Kou, L. Lam, Compressive strength, chloride diffusivity and pore structure of high performance metakaolin and silica fume concrete, Construction and Building Materials 20 (10) (2006) 858 – 865.

[7] M.-H. Zhang, H. Li, Pore structure and chloride permeability of concrete containing nano-particles for pavement, Construction and Building Materials 25 (2) (2011) 608 – 616.

[8] P. Duan, Z. Shui, W. Chen, C. Shen, Effects of metakaolin, silica fume and slag on pore structure, interfacial transition zone and compressive strength of concrete, Construction and Building Materials 44 (2013) 1 – 6.

[9] H. Ma, B. Xu, J. Liu, H. Pei, Z. Li, Effects of water content, magnesia-to-phosphate molar ratio and age on pore structure, strength and permeability of magnesium potassium phosphate cement paste, Materials & Design 64 (2014) 497 – 502.

[10] C. Atzeni, L. Massidda, U. Sanna, Effect of pore size distribution on strength of hardened cement pastes, in: Proceedings of the first international RILEM congress on pore structure and material properties, 1987, pp. 195 – 202.

[11] M.Y. Balshin, Dependence of the mechanical properties of powder metals on the porosity and the ultimate properties of powder cermet materials, Doklady Akademii Nauk SSSR 67 (5) (1949) 831 – 834.

[12] E. Ryshkewitch, Compression strength of porous sintered alumina and zirconia, Journal of the American Ceramic Society 36 (2) (1953) 65 – 68.

[13] K.K. Schiller, Porosity and strength of brittle solids, in: Mechanical Properties of Non-Metallic Brittle Materials, Butterworths, 1958, pp. 35 – 49.

[14] D.P.H. Hasselman, Relation between effects of porosity on strength and

on Young's modulus of elasticity of polycrystalline materials, Journal of the American Ceramic Society 46 (11) (1963) 564 – 565.

[15] D. Li, Z. Li, C. Lv, G. Zhang, Y. Yin, A predictive model of the effective tensile and compressive strengths of concrete considering porosity and pore size, Construction and Building Materials 170 (2018) 520 – 526.

[16] X. Du, L. Jin, G. Ma, Macroscopic effective mechanical properties of porous dry concrete, Cement and Concrete Research 44 (2013) 87 – 96.

[17] M. Pigeon, R. Pleau, Durability of concrete in cold climates, E & FN Spon, London, 1995.

[18] Y. Zhang, B. Yang, Z. Yang, G. Ye, Ink-bottle effect and pore size distribution of cementitious materials identified by pressurization–depressurization cycling mercury intrusion porosimetry, Materials 12 (9) (2019) 1454:1–15.

[19] P. Choi, J. H. Yeon, K.-K. Yun, Air-void structure, strength, and permeability of wet-mix shotcrete before and after shotcreting operation: The influences of silica fume and air-entraining agent, Cement and Concrete Composites 70 (2016) 69 – 77.

[20] R. Kumar, B. Bhattacharjee, Porosity, pore size distribution and in situ strength of concrete, Cement and concrete research 33 (1) (2003) 155 – 164.

[21] X. Wang, Y. Peng, J. Wang, Q. Zeng, Pore structure damages in cement-based materials by mercury intrusion: A non-destructive assessment by x-ray computed tomography, Materials 12 (14) (2019) 2220:1–16.

[22] S. Diamond, Mercury porosimetry: an inappropriate method for the measurement of pore size distributions in cement-based materials, Cement and concrete research 30 (10) (2000) 1517–1525.

[23] A.B. Abell, K.L. Willis, D.A. Lange, Mercury intrusion porosimetry and image analysis of cement-based materials, Journal of Colloid and Interface Science 211 (1) (1999) 39 – 44.

[24] M. A. Laskar, R. Kumar, B. Bhattacharjee, Some aspects of evaluation of concrete through mercury intrusion porosimetry, Cement and Concrete Research 27 (1) (1997) 93–105.

[25] N. Alderete, Y. Villagrán, A. Mignon, D. Snoeck, N. De Belie, Pore structure description of mortars containing ground granulated blast-furnace slag by mercury intrusion porosimetry and dynamic vapour sorption, Construction and Building Materials 145 (2017) 157–165.

[26] M. C. G. Juenger, H. M. Jennings, The use of nitrogen adsorption to assess the microstructure of cement paste, Cement and Concrete Research 31 (6) (2001) 883–892.

[27] F. Gong, D. Zhang, E. Sicat, T. Ueda, Empirical estimation of pore size distribution in cement, mortar, and concrete, Journal of materials in civil engineering 26 (7) (2014) 04014023.

[28] K. L. Scrivener, P. Pratt, Backscattered electron images of polished cement sections in the scanning electron microscope, in: Proceedings of the International Conference on Cement Microscopy, 1984, pp. 145–155.

[29] R. S. Edwin, M. Mushthofa, E. Gruyaert, N. De Belie, Quantitative analysis on porosity of reactive powder concrete based on automated analysis of back-scattered-electron images, Cement and Concrete Composites 96 (2019) 1–10.

[30] E. Landis, A. Petrell, S. Lu, E. Nagy, Examination of pore structure using three-dimensional image analysis of microtomographic, Concrete Science and Engineering 2 (2000) 162–169.

[31] A. du Plessis, B.J. Olawuyi, W.P. Boshoff, S.G. le Roux, Simple and fast porosity analysis of concrete using x-ray computed tomography, Materials and structures 49 (1-2) (2016) 553–562.

[32] S. Lu, E. Landis, D. Keane, X-ray microtomographic studies of pore structure and permeability in portland cement concrete, Materials and structures 39 (6) (2006) 611–620.

[33] S. Häfner, S. Eckardt, T. Luther, C. Könke, Mesoscale modeling of concrete: Geometry and numerics, Computers & Structures 84 (2006) 450 – 461.

[34] P. Wriggers, S.O. Moftah, Mesoscale models for concrete: Homogenisation and damage behaviour, Finite Elements in Analysis and Design 42 (2006) 623 – 636.

[35] J.P.B Leite, V. Slowik, J. Apel, Computational model of mesoscopic structure of concrete for simulation of fracture processes, Computers and Structures 85 (2007) 1293–1303.

[36] X.Q. Zhou, H. Hao, Modelling of compressive behaviour of concrete-like materials at high strain rate, International Journal of Solids and Structures 45 (2008) 4648 – 4661.

[37] I. Comby-Peyrot, F. Bernard, P-O Bouchard, F. Bay, E. Garcia-Diaz, Development and validation of a 3d computational tool to describe concrete behaviour at mesoscale. application to the alkali-silica reaction, Computational Materials Science 46 (2009) 1163–1177.

[38] J. Unger, S. Eckardt, C. Könke, A mesoscale model for concrete to simulate mechanical failure, Computers and Concrete 8 (2011) 401–423.

[39] N. Benkemoun, A. Ibrahimbegovic, J-B Colliat, Anisotropic constitutive model of plasticity capable of accounting for details of meso-structure of two-phase composite material, Computers and Structures 90-91 (2012) 153–162.

[40] F. Montero-Chacón, J. Marín-Montín, F. Medina, Mesomechanical characterization of porosity in cementitious composites by means of a voxel-based finite element model, Computational Materials Science 90 (2014) 157 – 170.

[41] M. Hain, P. Wriggers, Numerical homogenization of hardened cement paste, Computational Mechanics 42 (2008) 197–212.

[42] T. T. Nguyen, H. H. Bui, T. D. Ngo, G. D. Nguyen, Experimental and numerical investigation of influence of air-voids on the compressive behaviour of foamed concrete, Materials & Design 130 (2017) 103 – 119.

[43] L.A. Feldkamp, L.C. Davis, J.W. Kress, Practical cone-beam algorithm, Journal of the Optical Society of America A 1 (6) (1984) 612 – 619.

[44] J. Schindelin, I. Arganda-Carreras, E. Frise, V. Kaynig, M. Longair, T. Pietzsch, S. Preibisch, C. Rueden, S. Saalfeld, B. Schmid, J.Y. Tinevez, D.J. White, V. Hartenstein, K. Eliceiri, P. Tomancak, A. Cardona, Fiji: an open-source platform for biological-image analysis, Nature Methods 9 (7) (2012) 676 – 682.

[45] DIPimage toolbox for Matlab (http://www.diplib.org/), Delft University of Technology, Netherlands.

[46] ABAQUS/Standard version 2018 documentation, Dassault Systèmes Simulia Corp, United States, 2017.

[47] J. Lubliner, J. Oliver, S. Oller, E. Oñate, A plastic-damage model for concrete, International Journal of Solids and Structures 25 (3) (1989) 299 – 326.

[48] J. Lee, G.L. Fenves, Plastic-damage model for cyclic loading of concrete structures, Journal of Engineering Mechanics 124 (8) (1998) 892–900.

[49] C.G. Koh, M.Q. Teng, T.H. Wee, A plastic-damage model for lightweight concrete and normal weight concrete, International Journal of Concrete Structures and Materials 2 (2) (2008) 123–136.

[50] Y.-T. Jiao, B. Wang, Z.-Z. Shen, A new 3D empirical plastic and damage model for simulating the failure of concrete structure, International Journal of Concrete Structures and Materials 13 (57) (2019) 1–18.

[51] A.S. Genikomsou, M.A. Polak, Finite element analysis of punching shear of concrete slabs using damaged plasticity model in ABAQUS, Engineering Structures 98 (2015) 38 – 48.

[52] G. Duvaut, J.L. Lions, Les inéquations en mécanique et en physique, Dunod, Paris, France, 1972.

[53] M. Kõrgesaar, J. Romanoff, Influence of mesh size, stress triaxiality and damage induced softening on ductile fracture of large-scale shell structures, Marine Structures 38 (2014) 1 – 17.

[54] R. Vignjevic, N. Djordjevic, T.D. Vuyst, S. Gemkow, Modelling of strain softening materials based on equivalent damage force, Computer Methods in Applied Mechanics and Engineering 335 (2018) 52 – 68.

[55] E. Edalati, S. Sajjadi, A. Babakhani, Effects of SiC nanoparticles on the properties of titanium-matrix foams processed by powder metallurgy, Metals 7 (2017) 296:1–9.

[56] A. Amri, G. Fathurrahman, A. Najib, E. Awaltanova, A. Syamsuddin, C. Mukiyat, Composites of palm oil fuel ash (POFA) based geopolymer and graphene oxide: structural and compressive strength, IOP Conference Series: Materials Science and Engineering 420 (2018) 012063:1–6.

[57] L. N. Schaefer, J. E. Kendrick, T. Oommen, Y. Lavallée, G. Chigna, Geomechanical rock properties of a basaltic volcano, Frontiers in Earth Science 3 (2015) 29:1–15.

[58] E.P Kearsley, P.J Wainwright, The effect of porosity on the strength of

foamed concrete, Cement and Concrete Research 32 (2) (2002) 233 – 239.

[59] Y.-X. Li, Y.-M. Chen, J.-X. Wei, X.-Y. He, H.-T. Zhang, W.-S. Zhang, A study on the relationship between porosity of the cement paste with mineral additives and compressive strength of mortar based on this paste, Cement and Concrete Research 36 (9) (2006) 1740 – 1743.